Climate Dynamics (2024) 62:5019–5028
https://doi.org/10.1007/s00382-024-07148-8

ORIGINAL ARTICLE

Variability of the M_2 internal tides in the Luzon Strait under climate change

Zheng Guo[1] · Shuya Wang[2] · Anzhou Cao[3] · Xu Chen[4] · Jinbao Song[3] · Xinyu Guo[2]

Received: 24 September 2023 / Accepted: 6 February 2024 / Published online: 15 March 2024

Abstract
Internal tides (ITs) radiated from the Luzon Strait (LS) to the South China Sea (SCS) exhibit variability closely related to changes of stratification. Based on the CanESM5 simulation from the sixth phase of Coupled Model Intercomparison Project, the stratification within the LS will increase in the following century due to climate change resulting from human activities. Here we conduct numerical experiments to investigate changes of the M_2 ITs under different shared socioeconomic pathway (SSP) scenarios. Results show that the cumulative generation of ITs within the LS weakens with strengthening stratification. The amount of ITs generated in the LS will decrease by 22.7% (2.7%) and that propagating into the SCS will decrease by 27.9% (4.4%) in a century under the SSP5-8.5 (SSP1-2.6) scenario that represents the high (low) end of future emissions. The changes are attributed to the interference of the M_2 ITs within the double ridges, which weakens as the stratification strengthens and finally reduces the IT generation. Considering that ITs are one of the most important energy sources for diapycnal mixing, the decrease in ITs would have significant physical and biogeochemical implications in the LS and the SCS.

Keywords Internal tides · Luzon Strait · Climate change · Numerical simulation

1 Introduction

Internal tides (ITs) are generated in stratified waters when barotropic tidal currents interact with variable bottom topography (Garrett and Kunze 2007). Some fraction of ITs is dissipated locally near the generation sites (Klymak et al. 2008; Alford et al. 2011; Cao et al. 2023a), while the remaining part could propagate thousands of kilometers away (Zhao 2014), losing energy via processes such as topographic scattering and reflection (Müller and Xu 1992) and nonlinear transfer to smaller-scale waves (MacKinnon et al. 2013; Wang et al. 2021). Consequently, ITs play an important role in dissipating surface tidal energy and enhancing mixing (Rudnick et al. 2003; Tanaka 2023). It is estimated that ~ 1.0 TW ITs coming from tide-topography interaction in the deep ocean contribute approximately half of the energy required to fuel global turbulent dissipation and overturning (Munk and Wunsch 1998; Waterhouse et al. 2014; Kunze 2017). The magnitude and geography of IT mixing influence the global climate, including the global oceanic overturning circulation, water property distribution, and air-sea interactions (Whalen et al. 2020; Tanaka et al. 2014). The biogeochemical influence of ITs has also been increasingly recognized. In the deep basin, internal solitary waves induced by ITs result in phytoplankton flourishment because nutrient-replete waters are brought to the euphotic zone (Li et al. 2018). More attention has been put on the marginal seas, where breaking ITs increase the vertical fluxes of nutrients into the photic zone (Tweddle et al. 2013), and contribute to structuring plankton communities and supporting commercially-important fisheries (Sharples and Zeldis 2021). Moreover, as a ubiquitous motion in the global ocean, ITs also have major effects on acoustic transmission (Dushaw 2006) and oil-drilling platforms (Osborne and Burch 1980).

The Luzon Strait (LS) is one of the most active ITs generation sites around the world due to its characteristic double meridional ridges, strong stratification and intensive

✉ Anzhou Cao
caoanzhou@zju.edu.cn

1 Marine Science and Technology College, Zhejiang Ocean University, Zhoushan, China

2 Center for Marine Environmental Studies, Ehime University, Matsuyama, Japan

3 Ocean College, Zhejiang University, Zhoushan, China

4 Key Laboratory of Physical Oceanography, Ocean University of China, Qingdao, China

astronomical tides (Simmons et al. 2004; Alford et al. 2011). The ITs originating from the LS propagate eastwards into the Western Pacific and westwards into the South China Sea (SCS). They enhance the diapycnal mixing in the LS and the SCS, which influences the SCS circulation and maintains the abyssal water transport through the LS (Wang et al 2016). Ecologically, in addition to increasing nutrient transport and chlorophyll a, ITs in the SCS provide reefs thermal refugia from future global warming by regularly flushing them with cooler waters (Storlazzi et al. 2020).

In light of ITs' significant oceanographic effect, it's important to understand their changes. ITs in the SCS show a temporal variation on different scales. Based on satellite altimetry data from 1993 to 2017, Zhao and Qiu (2023) revealed significant seasonal variation in ITs from the LS: the westward ITs strengthen (weaken) in summer and fall (winter and spring); the opposite is true for the eastward ITs. The ocean stratification, besides the Kuroshio current, plays a critical role in the changes of ITs. On the multi-year scale, Zhai et al. (2020) found the diurnal and semidiurnal ITs in the SCS were negatively and positively correlated with the Niño 3.4 Index, respectively. The link between El Niño–Southern Oscillation (ENSO) and ITs is stratification. The stratification depends on the oceanic pressure, salinity, and temperature that are under influence of the human-induced climate change. The global stratification has strengthened by 5.3% during 1960–2018 (Li et al. 2020) and is expected to continue its increase trend in this century (Fu et al. 2016; Moore et al. 2018).

The primary goal of this study is to explore how ITs will be affected by global warming. The paper is organized as follows. The data used to analyze projected ocean stratification, the description and settings of models, as well as the methodology for analyzing ITs are presented in Sect. 2. In Sect. 3, we analyze the variations in stratification and ITs' energetics between the present and the future. The mechanism of ITs variation in the LS is discussed in Sect. 4. The final section provides a summary for the paper.

2 Data and methods

2.1 Data for stratification analysis

In this study, we use simulation data under two shared socioeconomic pathways (SSPs) scenarios, i.e., SSP1-2.6 and SSP5-8.5, from CanESM5, one of the models that participate in the sixth phase of Coupled Model Intercomparison Project (CMIP6). CMIP6 is a coordinated international effort to understand climate change arising from natural, unforced variability or in response to changes in radiative forcing (Eyring et al. 2016). Among all scenarios included in the CMIP6-endorsed Scenario Model Intercomparison Project, SSP1-2.6 represents the low end of the range of future forcing pathways and is expected to create a multi-model mean warming of much less than 2 °C by 2100. On the other end of the range of future pathways is SSP5-8.5 where climate change mitigation challenges dominate and a radiative forcing of 8.5 W m^{-2} in 2100 is produced (O'Neill et al. 2016). The ocean component of the CanESM5 model output has 45 vertical levels, varying in thickness from ~ 6 m near the surface to ~ 250 m in the abyssal ocean. Its horizontal resolution is based on a 1° Mercator grid, with a refinement of the meridional grid spacing to 1/3° near the Equator (Swart et al. 2019a). Based on the CMIP6 CanESM5 data (r1i1p1f1; Swart et al. 2019b), the ocean stratification is quantified by the buoyancy frequency

$$N = \sqrt{\frac{-g}{\rho_0}\frac{\partial \rho}{\partial z}}, \tag{1}$$

where g is gravitational acceleration, ρ is density, ρ_0 is the depth-averaged density, and z is depth.

2.2 Description and settings of the Coastal and Regional Ocean COmmunity (CROCO) model

The CROCO model is used to explore the changes in ITs generation under different scenarios. Based on the regional ocean modelling system from Institut de Recherche pour le Developpement (ROMS_AGRIF), CROCO solves the original governing equations under the hydrostatic equilibrium and Boussinesq approximation by default. The vertical turbulent mixing of momentum and tracers is parameterized by the Large-McWilliams-Doney k-profile scheme (Large et al. 1994) and the subgrid-scale turbulence is parameterized by the Laplacian horizontal mixing of momentum.

The simulation domain covers the northern SCS and part of the Philippine Sea from 115.5 to 126.5°E and 16–26°N (Fig. 1a). The bathymetry is extracted from the 1-min gridded elevations/bathymetry for the world (ETOPO1) data (Amante and Eakins 2009) and smoothed to minimize the horizontal pressure gradient errors. The grid spacing is 1/20° (approximately 5 km). The water column is divided into 25 uneven sigma layers in the vertical direction with finer resolution near the surface and bottom. The focus of this study is put on the generation of M_2 ITs. Therefore, at the four open boundaries, the surface elevations and barotropic currents of the M_2 tide are extracted from the Oregon State University Ocean Topography Experiment TOPEX/Poseidon Global Inverse Solution (TPXO7.2; Egbert and Erofeeva 2002) to force the model. The Flather condition is used for the barotropic currents and the radiative condition for the baroclinic currents at the open boundaries. In addition, a sponge layer spanning 0.5° is set to absorb the baroclinic energy and

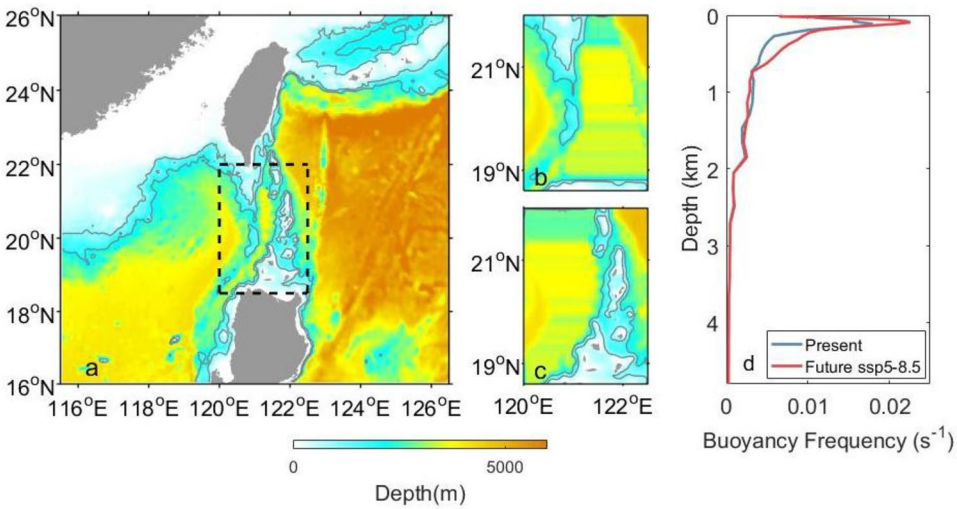

Fig. 1 **a** Depth of the simulation domain (shading, unit: m), with realistic bathymetry of double ridges in the LS. The gray contours indicate 1000 m and 2000 m isobaths and the dashed box indicates the LS. The ideal bathymetry of the LS where **b** the east ridge or **c** the west ridge is removed. **c** The mean buoyancy frequency within the LS used for the Present and Future SSP5-8.5 cases in the Group 2 experiments

avoid reflection. The model configuration has been validated for studying the ITs in the SCS (Guo et al. 2023; Cao et al. 2022, 2023b).

To investigate changes of IT generation in a warming ocean, we conduct three experiments (Group 1), i.e., the Present case, Future SSP1-2.6 case, and Future SSP5-8.5 case. Their initial fields are provided by the annual temperature, salinity, and currents from the SSP1-2.6 simulation of 2015, the SSP1-2.6 simulation of 2101, and the SSP5-8.5 simulation of 2101, respectively. The model is operated for 40 days to ensure that both the background field and the ITs reach a steady state. The simulated data are output every hour and those in the last 50 h (four M_2 tidal periods) are used for analysis.

A second group of experiments (Group 2) is conducted based on the CROCO model to further investigate the mechanism behind changes in ITs generation within the LS against global warming. Two cases are considered: the present and the future SSP5-8.5 cases. Their initial states are set to be horizontally homogenous and vertically stratified without background flows. Their stratifications are prescribed with data extracted from the SSP1-2.6 simulation of 2015 and SSP5-8.5 simulation of 2101, respectively (Fig. 1d). Specifically, they are calculated by averaging the annual temperature and salinity within the LS. In each case, simulation is conducted over three bathymetries, i.e., double ridges, single west ridge, and single east ridge in the LS (Fig. 1a–c). The model is operated for 15 days. The simulated data in the last 50 h (four M_2 tidal periods) are used for analysis.

2.3 IT energetics analysis

The barotropic to baroclinic energy conversion rate E_{bt2bc} is calculated by multiplying the pressure perturbation p' by the vertical barotropic velocity w_{bt} at the sea floor:

$$E_{\mathrm{bt2bc}} = p'(-H,t)w_{\mathrm{bt}}(-H,t). \tag{2}$$

In this study, the tidal-period-averaged conversion rate is calculated following Zilberman et al. (2011):

$$< E_{\mathrm{bt2bc}} >= 0.5p'(-H)w_{\mathrm{bt}}(-H)\cos(\theta_p - \theta_w), \tag{3}$$

where $p'(-H)$, $w_{\mathrm{bt}}(-H)$, θ_{p} and θ_{w} are the amplitudes and phases of the pressure perturbation and vertical barotropic velocity at the sea floor, respectively. Following Nash et al. (2005), the pressure perturbation is

$$p'(z,t) = \int_z^{\eta} \rho'(\hat{z},t)g\mathrm{d}\hat{z} - \frac{1}{H+\eta}\int_{-H}^{\eta}\int_z^{\eta} \rho'(\hat{z},t)g\mathrm{d}\hat{z}dz, \tag{4}$$

where ρ' is the density perturbation, and g is the acceleration due to gravity. According to Kerry et al. (2014, 2016), the depth-integrated baroclinic energy flux is

$$F_{bc} = \int_{-H}^{\eta} p'(z,t)u'(z,t)\mathrm{d}z, \tag{5}$$

where u' is the horizontal baroclinic velocity which is obtained by removing the time-averaged horizontal velocity and depth-averaged horizontal velocity from the instantaneous horizontal velocity.

2.4 Calculation of phase speed

The phase speed c_p can be derived from the eigenspeed (Zhao et al. 2010)

$$c_p = \frac{\omega}{(\omega^2 - f^2)^{\frac{1}{2}}}c_n, \tag{6}$$

where ω is the frequency of the M_2 tide, f is the local Coriolis frequency, and c_{n} is the eigenspeed that satisfies the Taylor–Goldstein equation (Xu et al. 2021)

$$\frac{\mathrm{d}^2\hat{w}}{\mathrm{d}z^2} + \left[\frac{N^2}{\left(U-c_n\right)^2} - |\mathbf{k}|^2 - \frac{\mathrm{d}^2U/\mathrm{d}z^2}{U-c_n}\right]\hat{w} = 0, \tag{7}$$

where $\hat{w}$ is the eigenfunction of vertical velocity, U is the background flow component parallel to the ITs direction, and $\mathbf{k}=(k, l)$ is the horizontal wave number. In this study, the Taylor–Goldstein equation is solved following Smyth et al. (2011) using his Matlab tool.

3 Results

3.1 Changes in stratification

Because LS is the IT generation site of interest, we focus on stratification variation within LS (120°E–122.5°E, 18.5°N–22°N) during approximate a century (2015–2110). The LS-averaged annual sea surface temperature (SST) is first inspected. In the SSP1-2.6 and SSP5-8.5 scenarios, the time series of SST show a similar trend until approximate 2040, increasing linearly at rates of 0.2 ℃ and 0.3 ℃ per decade, respectively (Fig. 2a). Thereafter, the SST stops rising under the SSP1-2.6 scenario and fluctuates between 28.2 and 29.3 ℃. However, under the SSP5-8.5 scenario, the surface warming intensifies at a rate of 0.5 ℃ per decade. The annual SST in 2110 reaches 33.0 ℃, which is 5.3 ℃ higher than that in 2015.

Attention is then paid to the changes in the stratification, which plays an important role in the generation of ITs. Compared with the annual stratification profile in 2015 derived from the SSP1-2.6 simulation, the stratification anomaly in the upper 800 m under the SSP1-2.6 scenario shows a three-layer structure: the layer between 100 and 200 m of negative anomaly is sandwiched between two layers of positive anomaly (Fig. 2c). Under the SSP5-8.5 scenario, the stratification anomaly also shows a three-layer pattern (Fig. 2d). However, the middle layer of negative anomaly becomes thinner towards the end of the twenty-first century and finally vanishes because the stratification intensifies across the whole water column. The upper layer of positive anomaly in the 100 m near the surface shows the strongest increasing trend with a rate of 2.5×10^{-3} s^{-1} per century, followed by the lower layer (200–800 m) with a rate of 2.2×10^{-3} s^{-1} per century, and the middle layer with a rate of 1.5×10^{-3} s^{-1} per century. Averaged vertically, the variation of buoyancy frequency in the upper 800 m within the LS (Fig. 2b) shows a similar pattern to the SST (Fig. 2a). In the first two decades, the mean buoyancy frequencies under the two scenarios are comparable. However, after 2040, the mean stratification remains relatively stable under the SSP1-2.6 scenario but shows a linear increase at a rate of

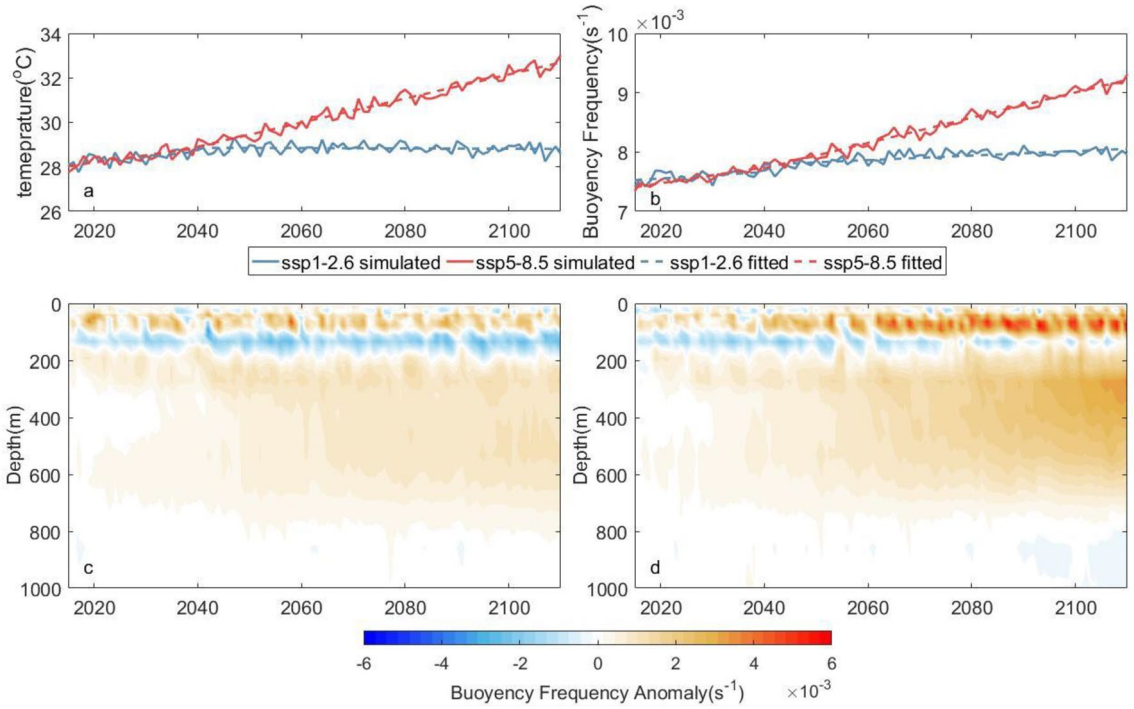

Fig. 2 Temporal changes in the annual **a** SST and **b** mean buoyancy frequency in the upper 800 m averaged within the LS in the SSP1-2.6 and SSP5-8.5 scenarios. The solid lines indicate results from the CanESM5 simulation and the dashed lines indicate their linear trend fitted during two periods (2015–2040 and 2040–2110) separately. Time series of the stratification anomalies under the **c** SSP1-2.6 and **d** SSP5-8.5 scenarios relative to the 2015 stratification profile derived from the SSP1-2.6 simulation

2.13×10^{-3} s^{-1} per century under the SSP5-8.5 scenario. The averaged stratification of the upper 800 m waters increases by 7.4% and 26.8% from 2015 to 2110 under the SSP1-2.6 and SSP5-8.5 scenarios, respectively.

3.2 IT energy budgets

Simulation results of the Present case in Group 1 experiment are first examined. The two ridges in the LS are important generation sites of the M_2 ITs (Fig. 3a). Particularly, the conversion rates over the east flank of the west ridge and the west flank of the east ridge exceed 1 W/m^2. The conversion rate integrated over the LS is 17.49 GW. Breaking down the total ITs generation to the west and east ridges yields 8.47 GW and 9.02 GW, respectively. These results are consistent with previous studies (Niwa and Hibiya 2004; Kerry et al. 2016; Xu et al. 2016).

The generation of the M_2 ITs shows a decreasing trend with global warming (Fig. 3b, c). Under the SSP1-2.6 scenario, the total generation of the M_2 ITs decreases by 2.7% from 17.49 to 17.02 GW in a century. The conversion rates integrated over west and east ridges show 1.2% and 4.2% decreases, respectively. Further inspection of the distribution of conversion rates shows that the amount of ITs generated decreases in most areas of the middle LS. However, an increase in conversion rates is also noticed, especially in the northern part of the west ridge. Changes in conversion rates are more significant under the SSP5-8.5 scenario where the stratification shows a more remarkable change than that under the SSP 1–2.6 scenario (Fig. 2b). Although the generation of ITs strengthens in some areas, sharp decreases are seen in the middle LS. Particularly, the decrease exceeds 50% over the west flank of the west ridge and the east flank of the east ridge. Integrated over the west and east ridges, the conversion rates show 19.0% and 26.2% decreases, respectively. The ITs generated over the LS is 13.52 GW, amounting to a 22.7% decrease from the Present case.

A large fraction of energy radiates away from the LS. Figure 4a shows that the pattern of depth-integrated energy flux of the M_2 ITs is consistent with previous studies (Niwa and Hibiya 2004; Zhao 2014; Alford et al. 2015). In the Present case, the energy of the M_2 ITs propagating westwards and eastwards out of the LS is 4.35 GW and 4.67 GW, respectively. The ITs into the SCS bifurcate into two beams: one propagates westwards along 21°N and the other propagates southwestwards. The ITs in the Philippine Sea are radiated eastwards with a wider beam. The patterns of energy flux in the Future cases are similar to that in the present (not shown). However, a reduction in barotropic to baroclinic energy conversion rates results in a reduction in energy flux received by the SCS and the Philippine Sea (Fig. 4b, c). Under the SSP1-2.6 scenario, the westward ITs energy flux decreases by 7.1% to 4.05 GW, while the eastward fluxes change very slightly. Under the SSP5-8.5 scenario, however, all the three main ITs beams weaken significantly, resulting in sharp decreases of 30.9% and 25.3% in the ITs moving westwards and eastwards out of the LS, respectively.

3.3 IT phase speed

Considering both stratification and mean flow in the Present case, the phase speed of mode-1 M_2 ITs in the water deeper than 1000 m in the SCS is approximate 2.89 m/s and that in the Philippine Sea is 3.43 m/s (Fig. 5a). Projected climate change in the ocean results in increase in the phase speed (Fig. 5b, c). Under the SSP1-2.6 scenario, the phase speeds averaged over the waters deeper than 1000 m increase by 0.16 m/s. Under the SSP5-8.5 scenario, the mean increase reaches 0.43 m/s. These results suggest that the climate change speeds up the propagation of the M_2 ITs near the LS.

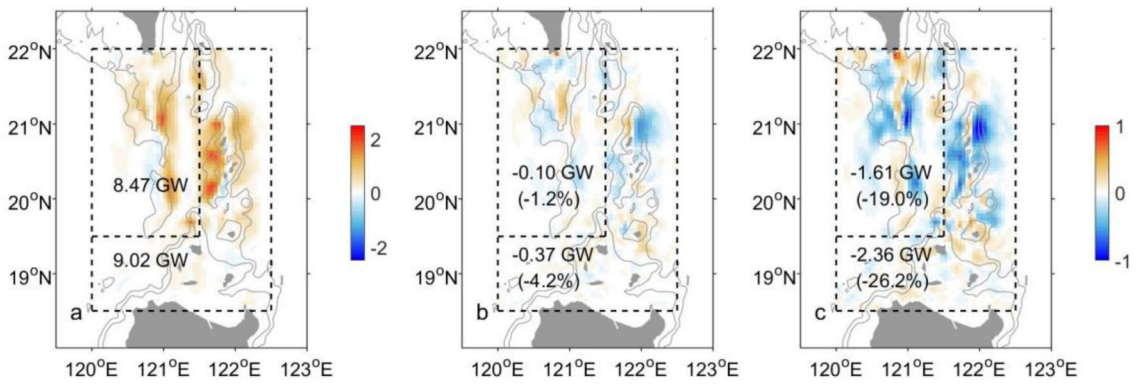

Fig. 3 **a** Energy conversion rates of the M_2 ITs (shading, unit: W/m^2) in the present and its difference with those in the future (Future case minus Present case) under the **b** SSP1-2.6 and **c** SSP5-8.5 scenarios. The numbers in **a** are the conversion rates integrated over the west and east ridges indicated by dashed lines. The numbers in **b** and **c** are the absolute difference in integrated conversion rates between the Future and Present cases and the numbers in brackets indicate the relative difference. Gray contours denote 1000 m and 2000 m isobaths

The separate contributions of the stratification and background flow to changes of phase speed are evaluated for the Future SSP5-8.5 case. Figure 6a shows that the phase speed of the mode-1 M_2 IT changes very slightly if only the variation in background flow is considered. In the deep basins, the changes are generally within ± 0.1 m/s. The phase speed in the water deeper than 1000 m in the SCS is approximate 2.91 m/s and that in the Philippine Sea is 3.45 m/s, which are nearly the same with the Present case. On the contrary, if only the variation of stratification is considered, the phase speed changes significantly (Fig. 6b), showing a similar pattern to that when both background flow and stratification are considered simultaneously (Fig. 5c). The increase of phase speed averaged over the simulation domain is 0.39 m/s, contributing 91% of the mean increase in the Future SSP5-8.5 case.

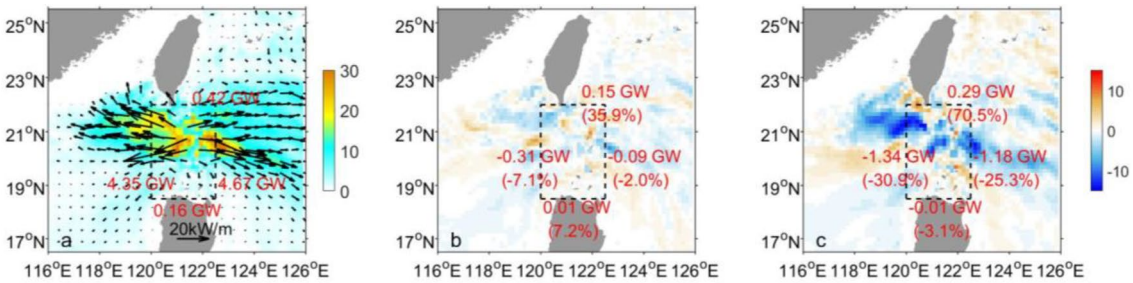

Fig. 4 **a** Depth-integrated energy flux of the M_2 ITs in the Present case and its difference with those in the Future (Future case minus Present case) under the **b** SSP1-2.6 and (c) SSP5-8.5 scenarios. The energy flux is shown by quivers and their magnitude is indicated by shading (unit: kW/m). The numbers in **a** are the energy flux integrated along the four boundaries of LS. The numbers in **b** and **c** are the absolute difference in integrated energy flux between the Future and Present cases and the numbers in brackets indicate the relative difference

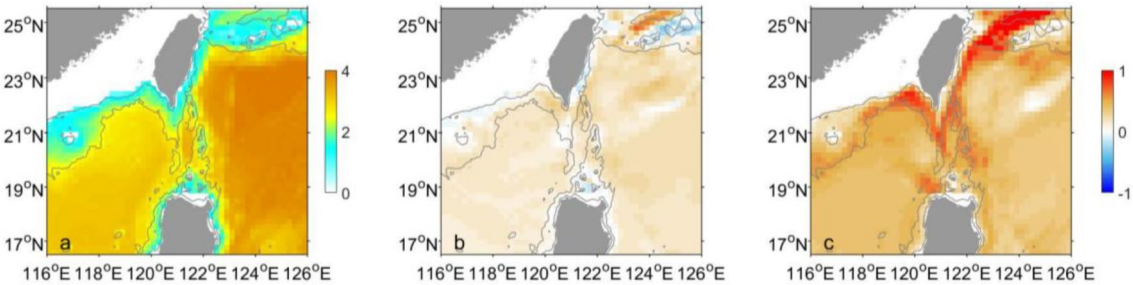

Fig. 5 **a** The phase speed of the mode 1 M_2 IT (shading, unit: m/s) in the Present case and its difference with those in the future (Future case minus Present case) under the **b** SSP1-2.6 scenario and **c** SSP5-8.5 scenario. Gray contours indicate the 200 m and 2000 m isobaths. Calculation is only conducted for areas with a depth larger than 200 m

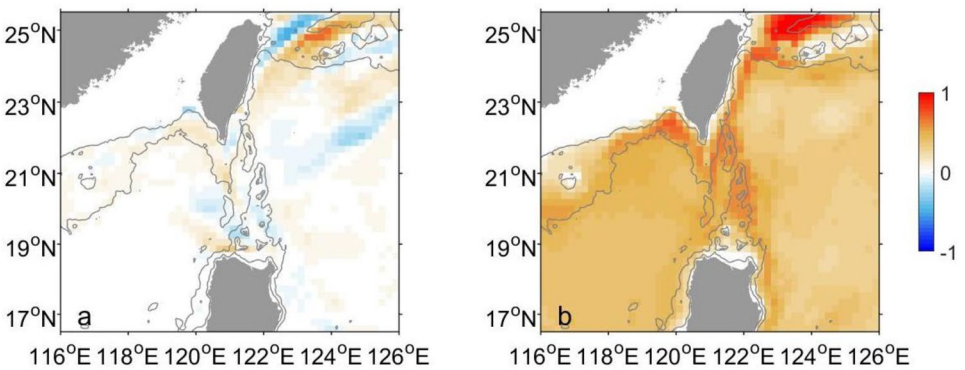

Fig. 6 The difference in phase speed of the mode 1 M_2 IT (shading, unit: m/s) between the future SSP5-8.5 case and the present case (future case minus present case) calculated merely considering the changes of **a** background flow or **b** stratification. Gray contours indicate the 200 m and 2000 m isobaths. Calculation is only conducted for areas with a depth larger than 200 m

4 Discussion

Results presented in Sect. 3 show that the IT generation in the LS will be weakened as the ocean warms (stratification increases). It seems contradictory to the projection by the equation of 'Baines force' (DeCarlo et al 2015), which indicates that the conversion of barotropic to baroclinic tides is directly proportional to N^2. The numerical simulation in the Andaman Sea also shows that ITs generation will be enhanced by the increase in stratification (Yadidya and Rao 2022).

However, it might not be the case in the LS. Zhao and Qiu (2023) stated that the IT generation and ocean stratification do not have a linear relation based on the IT energy flux estimated from the satellite observation. Specifically, the ocean stratification in the LS is the strongest in summer and the weakest in winter, however, the westward (eastward) M_2 energy fluxes reach the strongest in fall (winter) and the weakest in spring (summer). Guo et al. (2020) also found that the M_2 tidal conversion in the LS in winter is larger than that in summer. To explore what happens within the LS in our simulation, we first extract the mean flow from the Present case and the Future cases under two scenarios in Group 1. As is displayed in Fig. 7, they have a similar pattern showing a strong northward Kuroshio passing the LS in a leaping path (Nan et al. 2011). The similarity in the mean flow indicates that the difference in barotropic to baroclinic energy conversion rates among the Group 1 experiments largely results from the stratification. Stratification variation could change the interference of ITs in the LS by influencing the wavelength of ITs and finally change the barotropic-to-baroclinic energy conversion. To validate the above speculation, we conduct the Group 2 experiments where the initial condition is set to be homogenous without background flow and the bathymetry of the LS is set to be realistic double ridges, single west ridge or single east ridge.

The conversion rate from barotropic to baroclinic energy in each experiment of Group 2 are shown in Fig. 8. The patterns of conversion rate in the double-ridge experiments are similar to their counterparts in Group 1. To quantify the variation under climate change, the conversion rate is integrated over the LS, showing that the amount of ITs generated decreases by 18.5% from 17.31 GW in the Present case to 14.11 GW in the Future SSP5-8.5 case. The variation is similar to that in Group 1 experiments, confirming that the ocean stratification contributes more to the ITs in the LS under the changing climate than the background flow. In the single ridge experiments, the changes of ITs generation with strengthening stratification are within merely 6% in terms of the integrated conversion rate. The amount of ITs generated on the west ridge changes from 4.38 to 4.15 GW; while on the east ridge, the ITs decrease from 7.67 to 7.39 GW. Further speculation on changes of conversion rates reveals that they are site-dependent, which may be related to the complex bathymetry of the three-dimensional ridges.

The sharper decrease of ITs generation in the double ridge experiments than in the single ridge experiments suggested influence of stratification variation on the interference of ITs. Buijsman et al. (2012, 2014) demonstrated that, due to the constructive interference of ITs from the parallel ridges within the LS, the barotropic-to-baroclinic energy conversion is stronger compared to

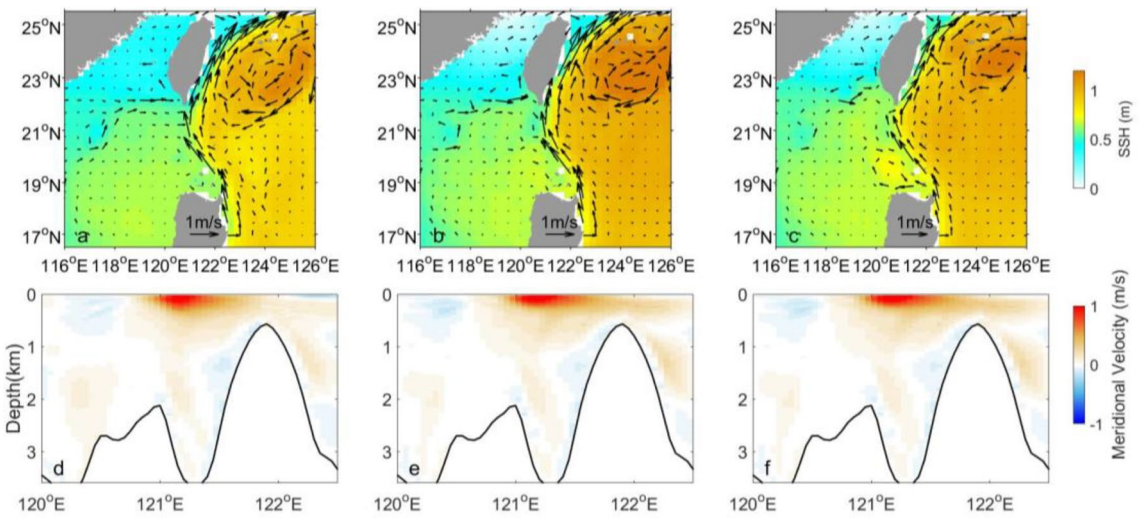

Fig. 7 The **a**–**c** sea surface height (SSH, shading, unit: m) and mean flow (arrows, unit: m/s) in the simulation domain and **d**–**f** the meridional velocity (shading, unit: m/s) along the 20.5°N transection in the LS extracted from the **a**, **d** present case, **b**, **e** future SSP1-2.6 case, and **c**, **f** future SSP5-8.5 case in Group 1

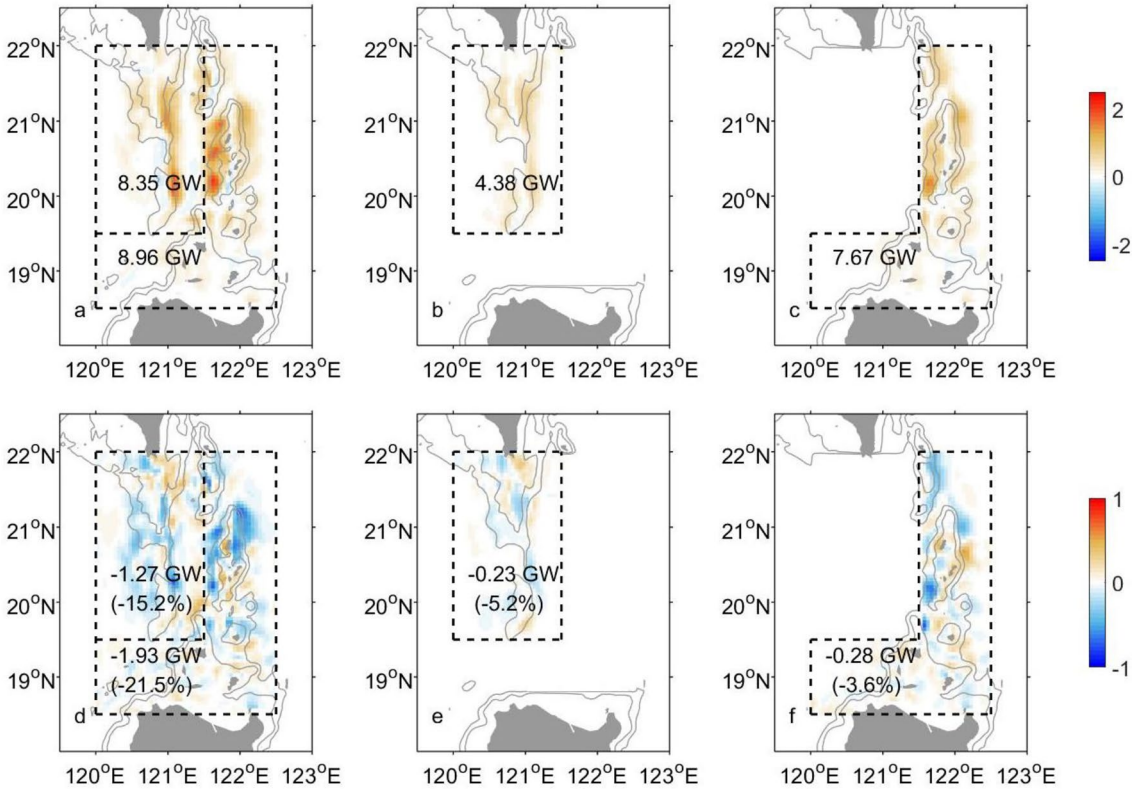

Fig. 8 **a**–**c** Energy conversion rates of the M_2 ITs (shading, unit: W/m^2) in the present and **d**–**f** its difference with those in the future (future case minus present case) on the bathymetry of **a**, **d** realistic double ridges, **b**, **e** single west ridge, and **c**, **f** single east ridge. The numbers in **a**–**c** are the conversion rates integrated over the west and east ridges indicated by dashed lines. The numbers in **d**–**f** are the absolute difference in integrated conversion rates between the future 5–8.5 and present cases and the numbers in brackets indicate the relative difference. Gray contours denote 1000 m and 2000 m isobaths

the sum of single ridge cases when semidiurnal tides are dominant. We measure the effect of interference in different cases by calculating the amplification ψ following Buijsman et al. (2012, 2014):

$$\psi = \frac{E_{\mathrm{DR}} - (E_{\mathrm{WR}} + E_{\mathrm{ER}})}{E_{\mathrm{WR}} + E_{\mathrm{ER}}}, \tag{8}$$

where subscripts WR, ER, and DR refer to the bathymetries of single west ridge, single east ridge, and double ridges. The amplifications in the present case and future 5–8.5 case are 0.44 and 0.22, respectively, which validates that the generation of the M_2 ITs decreases significantly because their constructive interference within the LS weakens as the stratification strengthens. The simulation explains to some extent why the IT generation within the LS weakens greatly as the stratification strengthens. However, the changes of the barotropic to baroclinic conversion rates are actually site-dependent (Fig. 8d). We believe that it is related to the interference of ITs over the three-dimensional bathymetry, which has been explored thoroughly in Buijsman et al. (2014).

5 Summary

ITs originating from the LS exhibit variations related to changes in stratification induced by seasonal changes and ENSO events. Based on the CanESM5 simulation from the CMIP6 project, we find that the stratification within the LS shows an increasing trend due to climate change resulting from human activities. More specifically, the stratification under the SSP5-8.5 scenario, which represents the high end of the range of future emissions, increases more significantly than that under the SSP1-2.5 scenario.

To investigate changes of the M_2 ITs under different SSP scenarios, we conduct experiments with the CROCO model. The results show that, the cumulative generation within the LS weakens with strengthening stratification, though changes of the energy conversion rates are site-dependent. In the beginning of the next century, under the SSP5-8.5 scenario, the amount of ITs generated will decrease by 22.7% from the present case, and ITs propagating out of the LS into the SCS will decrease by 27.9%. The changes of ITs under

the SSP1-2.6 scenario are much slighter. The results are different from the projection by the theory that the conversion of barotropic to baroclinic tides is directly proportional to N^2. The paradox could be explained by the interference of ITs within the LS due to its characteristic double ridges, which is proved by another group of CROCO simulation where the double-ridge bathymetry of the LS is changed.

Changes in the IT generation and propagation against climate change have significant implications. The ITs radiated from the LS are the dominant energy source for the tidal dissipation in the SCS (Wang et al. 2016). A sharp decrease in ITs will weaken diapycnal mixing in the domain, which will consequently influence the circulation in SCS and abyssal water transport through the LS. Near coasts where ITs break, nutrients delivered by ITs-induced mixing and subsequently growth of phytoplankton will decrease as ITs weaken. Moreover, the changes of ITs in the LS is different from those in the Andaman Sea where increase in stratification will enhance ITs generation (Yadidya and Rao 2022). It indicates that caution should be taken when predicting the changes of IT generation on a global scale under climate change. The site-dependent changes of ITs will yield a complex global geography of IT mixing. This pattern deserves more attention in the development of mixing parameterizations (Melet et al. 2016; Tatebe et al. 2018), because it affects the meridional overturning circulation and thus the broader global climate system (Whalen et al. 2020).

Acknowledgements This study is supported by the Bureau of Science and Technology of Zhoushan through the Zhejiang Ocean University Science and Technology Project (No. 2023C41012) and the National Natural Science Foundation of China (Grant Number: 42176002).

Author contributions A Cao and S Wang contributed to the study conception and design. Z Guo conducted numerical experiments, performed the analysis and wrote the first draft of the manuscript. All authors contributed to the discussions, commented on previous versions of the manuscript, read and approved the final manuscript.

Data availability CanESM5 data used in this study can be downloaded from the CMIP6 database at https://esgf-node.llnl.gov/projects/cmip6/.

Declarations

Conflict of interest The authors declare no competing interests.

Ethical approval Not applicable.

References

Alford MH, MacKinnon JA, Nash JD, Simmons H, Pickering A, Klymak JM, Musgrave R (2011) Energy flux and dissipation in Luzon Strait: two tales of two ridges. J Phys Oceanogr 41(11):2211–2222

Alford MH, Peacock T, MacKinnon JA, Nash JD, Buijsman MC, Centurioni LR, Fringer OB (2015) The formation and fate of internal waves in the South China Sea. Nature 521(7550):65

Amante C, Eakins BW (2009) ETOPO1 1 arc-minute global relief model: procedures, data sources and analysis. NOAA Technical Memorandum NESDIS NGDC-24. National Geophysical Data Center, NOAA

Buijsman MC, Legg S, Klymak J (2012) Double ridge internal tide interference and its effect on dissipation in Luzon Strait. J Phys Oceanogr 42:1337–2135

Buijsman MC, Klymak JM, Legg S, Alford MH, Farmer D, MacKinnon JA, Simmons H (2014) Three-dimensional double-ridge internal tide resonance in Luzon Strait. J Phys Oceanogr 44(3):850–869

Cao A, Guo Z, Wang S, Guo X, Song J (2022) Incoherence of the M2 and K1 internal tides radiated from the Luzon Strait under the influence of looping and leaping Kuroshio. Prog Oceanogr 206:102850

Cao A, Guo Z, Wang S, Chen X, Song J, Guo X (2023a) Energetics of the M2 internal tides modulated by typhoons at the Luzon Strait. Ocean Model 186:102243

Cao A, Guo Z, Wang S, Guo X, Song J (2023b) Numerical evaluation of internal tide characteristics extracted from mobile float observations: a case study near the Luzon Strait. J Atmos Ocean Technol 40(8):957–968

DeCarlo TM, Karnauskas KB, Davis KA, Wong GTF (2015) Climate modulates internal wave activity in the Northern South China Sea. Geophys Res Lett 42(3):831–838

Dushaw BD (2006) Mode-1 internal tides in the western North Atlantic Ocean. Deep Sea Res Part I 53(3):449–473

Egbert GD, Erofeeva SY (2002) Efficient inverse modeling of barotropic ocean tides. J Atmos Ocean Technol 19(2):183–204

Eyring V, Bony S, Meehl GA, Senior CA, Stevens B, Stouffer RJ, Taylor KE (2016) Overview of the Coupled Model Intercomparison Project Phase 6 (CMIP6) experimental design and organization. Geosci Model Dev 9(5):1937–1958

Fu W, Randerson JT, Moore JK (2016) Climate change impacts on net primary production (NPP) and export production (EP) regulated by increasing stratification and phytoplankton community structure in the CMIP5 models. Biogeosciences 13(18):5151–5170

Garrett C, Kunze E (2007) Internal tide generation in the deep ocean. Annu Rev Fluid Mech 39(1):57–87

Guo Z, Cao A, Lv X, Song J (2020) Impacts of stratification variation on the M2 internal tide generation in Luzon Strait. Atmos Ocean 58(3):206–218

Guo Z, Wang S, Cao A, Xie J, Song J, Guo X (2023) Refraction of the M2 internal tides by mesoscale eddies in the South China Sea. Deep Sea Res Part I 192:103946

Kerry CG, Powell BS, Carter GS (2014) The impact of subtidal circulation on internal tide generation and propagation in the Philippine Sea. J Phys Oceanogr 44(5):1386–1405

Kerry CG, Powell BS, Carter GS (2016) Quantifying the incoherent M2 internal tide in the Philippine Sea. J Phys Oceanogr 46(8):2483–2491

Klymak JM, Pinkel R, Rainville L (2008) Direct breaking of the internal tide near topography: Kaena Ridge. Hawaii J Phys Oceanogr 38(2):380–399

Kunze E (2017) Internal-wave-driven mixing: global geography and budgets. J Phys Oceanogr 47(6):1325–1345

Large WG, McWilliams JC, Doney SC (1994) Oceanic vertical mixing: a review and a model with a nonlocal boundary layer parameterization. Rev Geophys 32(4):363–403

Li D, Chou WC, Shih YY, Chen GY, Chang Y, Chow CH, Hung CC (2018) Elevated particulate organic carbon export flux induced by internal waves in the oligotrophic northern South China Sea. Sci Rep 8(1):2042. https://doi.org/10.1038/s41598-018-20184-9

Li G, Cheng L, Zhu J, Trenberth KE, Mann ME, Abraham JP (2020) Increasing ocean stratification over the past half-century. Nat Clim Change 10(12):1116–1123

MacKinnon JA, Alford MH, Pinkel R, Klymak J, Zhao Z (2013) The latitudinal dependence of shear and mixing in the pacific transiting the critical latitude for PSI. J Phys Oceanogr 43(1):3–16
Melet A, Legg S, Hallberg R (2016) Climatic impacts of parameterized local and remote tidal mixing. J Clim 29(10):3473–3500
Moore JK, Fu W, Primeau F, Britten GL, Lindsay K, Long M, Randerson JT (2018) Sustained climate warming drives declining marine biological productivity. Science 359(6380):1139–1143
Müller P, Xu N (1992) Scattering of oceanic internal gravity waves off random bottom topography. J Phys Oceanogr 22(5):474–488
Munk W, Wunsch C (1998) Abyssal recipes II: energetics of tidal and wind mixing. Deep Sea Res 45(12):1977–2010
Nan F, Xue H, Chai F, Shi L, Shi M, Guo P (2011) Identification of different types of Kuroshio intrusion into the South China Sea. Ocean Dyn 61(9):1291–1304
Nash JD, Alford MH, Kunze E (2005) Estimating internal wave energy fluxes in the ocean. J Atmos Ocean Technol 22(10):1551–1570
Niwa Y, Hibiya T (2004) Three-dimensional numerical simulation of M2 internal tides in the East China Sea. J Geophys Res 109:C04027
O'Neill BC, Tebaldi C, van Vuuren DP, Eyring V, Friedlingstein P, Hurtt G, Sanderson BM (2016) The scenario model intercomparison project (ScenarioMIP) for CMIP6. Geosci Model Dev 9(9):3461–3482
Osborne AR, Burch TL (1980) Internal solitons in the Andaman Sea. Science 208(4443):451–460
Rudnick DL, Boyd TJ, Brainard RE, Carter GS, Egbert GD, Gregg MC, Sanford TB (2003) From tides to mixing along the Hawaiian Ridge. Science 301(5631):355–357
Sharples J, Zeldis JR (2021) Variability of internal tide energy, mixing and nitrate fluxes in response to changes in stratification on the northeast New Zealand continental shelf. NZ J Mar Freshw Res 55(1):94–111
Simmons HL, Hallberg RW, Arbic BK (2004) Internal wave generation in a global baroclinic tide model. Deep-Sea Res Part II 51(25):3043–3068
Smyth WD, Moum JN, Nash JD (2011) Narrowband, high-frequency oscillations at the equator. Part II: properties of shear instabilities. J Phys Oceanogr 41:412–428
Storlazzi CD, Cheriton OM, van Hooidonk R, Zhao Z, Brainard R (2020) Internal tides can provide thermal refugia that will buffer some coral reefs from future global warming. Sci Rep 10(1):13435
Swart NC, Cole JNS, Kharin VV, Lazare M, Scinocca JF, Gillett NP, Winter B (2019a) The Canadian Earth System Model version 5 (CanESM5.0.3). Geosci Model Dev 12(11):4823–4873
Swart NC, Cole JNS, Kharin VV, Lazare M, Scinocca JF, Gillett NP, Sigmond M (2019b) CCCma CanESM5 model output prepared for CMIP6 Scenario MIP. Version 20190429. Earth System Grid Federation
Tanaka Y (2023) Energy conversion rate from subinertial surface tides to internal tides. J Phys Oceanogr 53(5):1355–1374
Tanaka Y, Yasuda I, Osafune S, Tanaka T, Nishioka J, Volkov YN (2014) Internal tides and turbulent mixing observed in the Bussol Strait. Prog Oceanogr 126:98–108
Tatebe H, Tanaka Y, Komuro Y, Hasumi H (2018) Impact of deep ocean mixing on the climatic mean state in the Southern Ocean. Sci Rep 8(1):1–9
Tweddle JF, Palmer MR, Davidson K, McNeill S (2013) Enhanced nutrient fluxes at the shelf sea seasonal thermocline caused by stratified flow over a bank. Prog Oceanogr 117:37–47
Wang X, Peng S, Liu Z, Huang RX, Qian Y-K, Li Y (2016) Tidal mixing in the South China Sea: An estimate based on the internal tide energetics. J Phys Oceanogr 46(1):107–124
Wang S, Cao A, Chen X, Li Q, Song J (2021) On the resonant triad interaction over mid-ocean ridges. Ocean Model 158:101734
Waterhouse AF, MacKinnon JA, Nash JD, Alford MH, Kunze E, Simmons HL, Lee CM (2014) Global patterns of diapycnal mixing from measurements of the turbulent dissipation rate. J Phys Oceanogr 44(7):1854–1872
Whalen CB, de Lavergne C, Naveira Garabato AC, Klymak JM, MacKinnon JA, Sheen KL (2020) Internal wave-driven mixing: governing processes and consequences for climate. Nat Rev Earth Environ 1(11):606–621
Xu Z, Liu K, Yin B, Zhao Z, Wang Y, Li Q (2016) Long-range propagation and associated variability of internal tides in the South China Sea. J Geophys Res Oceans 121(11):8268–8286
Xu Z, Wang Y, Liu Z, McWilliams JC, Gan J (2021) Insight into the dynamics of the radiating internal tide associated with the Kuroshio current. J Geophys Res Oceans 126(6):e2020JC017018
Yadidya B, Rao AD (2022) Projected climate variability of internal waves in the Andaman Sea. Commun Earth Environ 3(1):252
Zhai R-W, Chen G-Y, Liang C-R, Shang X-D, Xie J-S (2020) The Influence of ENSO on the Structure of Internal Tides in the Xisha Area. J Geophys Res Oceans 125(3):e2019JC015405
Zhao Z (2014) Internal tide radiation from the Luzon Strait. J Geophys Res Oceans 119(8):5434–5448
Zhao Z, Qiu B (2023) Seasonal West-East Seesaw of M2 internal tides from the Luzon Strait. J Geophys Res Oceans 128(3):e2022JC019281
Zhao Z, Alford MH, MacKinnon JA, Pinkel R (2010) Long-range propagation of the semidiurnal internal tide from the Hawaiian Ridge. J Phys Oceanogr 40(4):713–736
Zilberman N, Merrifield M, Carter G, Luther D, Levine M, Boyd T (2011) Incoherent nature of M 2 internal tides at the Hawaiian Ridge. J Phys Oceanogr 41(11):2021–2036